A Multimodel Intercomparison of an Intense Typhoon in Future, Warmer Climates by Four 5-km-Mesh Models

Sachie Kanada,[a] Tetsuya Takemi,[b] Masaya Kato,[a] Shota Yamasaki,[c]
Hironori Fudeyasu,[c] Kazuhisa Tsuboki,[a] Osamu Arakawa,[d] and Izuru Takayabu[e]

[a] Institute for Space-Earth Environmental Research, Nagoya University, Nagoya, Aichi, Japan
[b] Disaster Prevention Research Institute, Kyoto University, Uji, Kyoto, Japan
[c] Yokohama National University, Yokohama, Kanagawa, Japan
[d] University of Tsukuba, Tsukuba, Ibaraki, Japan
[e] Meteorological Research Institute, JMA, Tsukuba, Ibaraki, Japan

ABSTRACT

Intense tropical cyclones (TCs) sometimes cause huge disasters, so it is imperative to explore the impacts of climate change on such TCs. Therefore, the authors conducted numerical simulations of the most destructive historical TC in Japanese history, Typhoon Vera (1959), in the current climate and a global warming climate. The authors used four nonhydrostatic models with a horizontal resolution of 5 km: the cloud-resolving storm simulator, the fifth-generation Pennsylvania State University–National Center for Atmospheric Research Mesoscale Model, the Japan Meteorological Agency (JMA) operational nonhydrostatic mesoscale model, and the Weather Research and Forecasting Model. Initial and boundary conditions for the control simulation were provided by the Japanese 55-year Reanalysis dataset. Changes between the periods of 1979–2003 and 2075–99 were estimated from climate runs of a 20-km-mesh atmospheric general circulation model, and these changes were added to the initial and boundary conditions of the control simulation to produce the future climate conditions.

Although the representation of inner-core structures varies largely between the models, all models project an increase in the maximum intensity of future typhoons. It is found that structural changes only appeared around the storm center with sudden changes in precipitation and near-surface wind speeds as the radius of maximum wind speed (RMW) contracted. In the future climate, the water vapor mixing ratio in the lower troposphere increased by 3–4 $g\,kg^{-1}$. The increased water vapor allowed the eyewall updrafts to form continuously inside the RMW and contributed to rapid condensation in the taller and more intense updrafts.

1. Introduction

An increase in sea surface temperature (SST) is a known consequence of anthropogenic greenhouse warming (e.g., Collins et al. 2013; Mizuta et al. 2014). The SST increase projected by several state-of-the-art models implies a potential increase in tropical cyclone (TC) intensity in the future, warmer climate because the maximum intensity of a TC generally increases as SST increases (e.g., DeMaria and Kaplan 1994; Emanuel 1986, 1988; Holland 1997). Intense TCs such as Hurricane Katrina (2005) (Knabb et al. 2005), Typhoon Haiyan (2013) (Lin et al. 2013; Mori et al. 2014), and Cyclone Pam (2015) (Needham et al. 2015) have caused hugely destructive disasters in countries with exposed coasts. Thus, to prepare for future disasters, it is essential to understand how such intense TCs will change under future, warmer environmental conditions.

General circulation models (GCMs) with horizontal resolutions of several tens of kilometers have played a crucial role in projecting changes in the frequency, track, and location of occurrence of future TCs (e.g., Christensen et al. 2013; Stowasser et al. 2007; Murakami et al. 2012), but simulated TC intensity depends on model resolution, and it becomes more realistic when the resolution is increased (e.g., Bengtsson et al. 2007; Murakami and Sugi 2010; Roberts et al. 2015). TC intensity is closely related to TC inner-core structures. Sensitivity experiments of model resolutions on a simulated intense TC suggest that to simulate the maximum

---

ð Denotes content that is immediately available upon publication as open access.

Corresponding author: Sachie Kanada, skanada@nagoya-u.jp

intensity and inner-core structures of an intense TC, the horizontal resolution of the model should not exceed 5 km (e.g., Fierro et al. 2009; Kanada and Wada 2016).

In addition to resolution, projections of future TC intensity are affected by the model physics, such as the cumulus parameterization (e.g., Murakami et al. 2012) and the microphysics parameterization (e.g., McFarquhar et al. 2012; Zhu et al. 2015) schemes. The diffusion processes that determine the properties of the surface layer and the planetary boundary layer (PBL) are also crucial (Rotunno and Bryan 2012) because heat and moisture fluxes from the sea surface are major energy sources for TC development (e.g., Emanuel 1986; Rotunno and Emanuel 1987). Thus, the two major considerations in projections of future changes of an intense TC are the horizontal resolution and physics of the model.

One approach to increasing model resolution to study future changes in TC activity is to conduct dynamical downscaling experiments with regional models (e.g., Knutson et al. 2013, 2015). Knutson and Tuleya (1999) adopted this approach with a regional model with a horizontal resolution of 18 km; in simulations of 51 present-day cases and 51 future cases by GCMs, they showed that in the northwest Pacific, TC intensity and near-storm precipitation would significantly increase. Recently, 2-km-mesh nonhydrostatic models have been used for dynamical downscaling experiments to project the maximum intensity of intense TCs in the future climate (e.g., Kanada et al. 2013; Tsuboki et al. 2015). However, a limitation of the dynamical downscaling approach is that the boundary conditions of both the present-day and future cases are provided by the climate runs with GCMs. Therefore, it is important to discuss how actual intense TCs in the current climate will be changed in the future climate.

Another downscaling approach for examining the effect of future environments on TC intensity is to perform a conditional ensemble experiment. In this approach, a TC vortex is embedded in the initial and boundary conditions, and profiles of an environmental parameter, such as SST, moisture, or temperature, are varied (e.g., Knutson and Tuleya 2004; Knutson et al. 2001; Shen et al. 2000). Such conditional ensemble experiments can elicit the pure response of a TC vortex to a given environmental condition over a large parameter space. Hill and Lackmann (2011) performed 78 idealized simulations with a 6-km-mesh model and an additional six simulations with a 2-km-mesh model; in these simulations, they varied the future boundary conditions by using the output of 13 individual atmosphere–ocean GCM runs under different emission scenarios (A1B, B1, or A2), as well as the model physics, such as the surface layer–PBL scheme and the cloud microphysics

parameterization scheme, and then evaluated the effect of various changes in the thermodynamic environment on maximum TC intensity.

Most theoretical and numerical studies have suggested that in the future, TCs will most likely have increased maximum intensity and increased inner-core precipitation. These findings led us to pose the following question: How would a TC that was extremely intense in the current climate, such as Hurricane Katrina or Typhoon Haiyan, be changed in the future climate? To answer this question, the pseudo-global-warming (PW) method has been proposed (e.g., Kimura and Kitoh 2007). Although most conditional ensemble experiments are conducted as idealized experiments, the PW method involves dynamical downscaling experiments in which the boundary conditions are set by adding climate change differences between future and current climates simulated by GCMs to the real synoptic environment such as reanalysis datasets. This method has been widely applied in studies of the impacts of climate change on weather events, such as the rainy season in East Asia (i.e., the baiu; Kawase et al. 2009), extreme tornadic storm events (Trapp and Hoogewind 2016), and winter storm (Rasmussen et al. 2011) and flood events in North America (Lackmann 2013).

The PW method has also been used to study future changes in current intense TCs, including Hurricane Katrina (2005) (Lynn et al. 2009), Hurricane Sandy (2012) (Lackmann 2015), Typhoon Songda (2004) (Ito et al. 2016), and Typhoon Haiyan (2013) (Nakamura et al. 2016; Takayabu et al. 2015). However, most of these studies have focused on changes in maximum intensity and tracks and resultant natural disasters such as storm surges. The inner-core structures of a TC depend on its intensity and vary as the TC intensifies (e.g., Rogers et al. 2013). In particular, it is known that intense TCs intensify rapidly (Kaplan and DeMaria 2003). How will climate change affect the intensification process and cause a future TC to increase its maximum intensity?

To answer this question, we conducted PW experiments for Typhoon Vera (1959), the most destructive historical TC known, in both the current climate and the global warming climate. Typhoon Vera was an extraordinarily intense TC in which minimum central pressure (CP) reached 895 hPa. The typhoon struck Japan on 26 September 1959 and caused 5098 fatalities, making it the deadliest typhoon on record to make landfall in Japan. Because there are large uncertainties in TC representation by models and in model physics, we used four 5-km-mesh nonhydrostatic models with different physics schemes, the cloud-resolving storm simulator (CReSS), the Japan Meteorological Agency (JMA) operational nonhydrostatic mesoscale model

TABLE 1. Specifications of the models.

Models	CReSS	JMANHM	MM5	WRF
Vertical levels (top height)	80 (24 km)	55 (27 km)	55 (27 km)	56 (26 km)
Time step	4 s	15 s	4 s	20 s
Cumulus convection	None	Kain–Fritsch	Kain–Fritsch	Kain–Fritsch
Cloud microphysics	Simple two-moment three-ice bulk scheme	Simple two-moment three-ice bulk scheme	Goddard microphysics with hail–graupel	WRF single-moment 6-class microphysics scheme
Radiation	Tsuboki and Sakakibara (2002)	Yabu et al. (2005); Kitagawa (2000)	New Rapid Radiative Transfer Model	New Rapid Radiative Transfer Model
Turbulence/PBL scheme	Deardorff	Level 3 Mellor–Yamada–Nakanishi–Niino	Eta–Mellor–Yamada–Janjić	Yonsei University nonlocal
Surface boundary layer	Louis et al. (1982) with Kondo (1975)	Louis et al. (1982) with Kondo (1975)	Eta–Mellor–Yamada–Janjić	Zhang and Anthes (1982)
Nudging	Tsuboki and Sakakibara (2002)	Nakano et al. (2012)	Stauffer and Seaman (1990)	Wang et al. (2010)
Ocean	1D slab	None	None	None

(JMANHM), the fifth-generation Pennsylvania State University–National Center for Atmospheric Research Mesoscale Model (MM5), and the Weather Research and Forecasting (WRF) Model, and conducted PW experiments in which we paid special attention to structural changes of the inner core during the intensification period. The goal of this study was to examine how the inner-core structures of a simulated intense TC change in response to warmer climate conditions and how those changes lead to a maximum intensity increase.

The rest of the paper is organized as follows. Section 2 describes the models and the methodology. The environmental conditions used in the simulations of the current and future climates are summarized in section 3, and the results of the multimodel ensemble experiments are presented in section 4. The results are discussed in section 5, and section 6 is a summary.

2. Models and methodology

a. Model descriptions

We used four nonhydrostatic models, each with a horizontal resolution of 5 km: CReSS (Tsuboki and Sakakibara 2002); JMANHM (Saito et al. 2007); MM5 (Dudhia 1993; Grell et al. 1994); and WRF, version 3.3.1 (Skamarock et al. 2008) (Table 1). JMANHM, MM5, and WRF all use the Kain–Fritsch cumulus parameterization scheme (Kain and Fritsch 1993). Other model physics schemes that affect the simulated TC intensity are those related to the PBL and surface enthalpy fluxes. JMANHM applies a level 3 Mellor–Yamada–Nakanishi–Niino (MYNN) closure PBL scheme (Nakanishi and Niino 2004) and the Louis surface boundary layer scheme (Louis et al. 1982) with a surface-roughness-length

formulation based on Kondo (1975). WRF uses the Yonsei University nonlocal PBL scheme (Hong et al. 2006) with a surface boundary layer scheme based on Zhang and Anthes (1982). MM5 uses the Eta–Mellor–Yamada scheme (MYJ) developed by Janjić (1994), and CReSS uses the Louis surface boundary layer scheme (Louis et al. 1982) with a surface-roughness-length formulation based on Kondo (1975), but does not apply any parameterization for the PBL. Cloud–radiation interaction is not considered in CReSS, while long- and shortwave radiation processes at the surface are considered (Tsuboki and Sakakibara 2002). JMANHM (Nakano et al. 2012) and WRF (Wang et al. 2010) apply spectral nudging schemes developed for downscaling experiments, whereas MM5 and CReSS use an analysis nudging scheme (Stauffer and Seaman 1990). To make the initial spinup, the scheme in CReSS (MM5) was used for 72 h (36 h) from initial time. In addition, WRF can also use a tropical cyclone bogus scheme (TC bogus scheme; Wang et al. 2010). We conducted sensitivity experiments with the WRF Model that included the TC bogus scheme (WRFB). Among the four models, only CReSS considers the ocean effect. A simple thermal diffusion model (1D-slab model) is used to express temperature changes due to ocean mixing. The effect of ocean upwelling, however, is not included in the 1D-slab model. Hourly and 3-hourly outputs of all models were used for the surface and atmospheric analyses.

b. Experimental design

First, control simulations of Typhoon Vera in the current climate (CNTL) were performed with the four nonhydrostatic models using a horizontal resolution of 5 km (CNTL simulations). Initial and lateral atmospheric boundary conditions and SST were provided every 6 h from the Japanese 55-year Reanalysis (JRA-55; Kobayashi
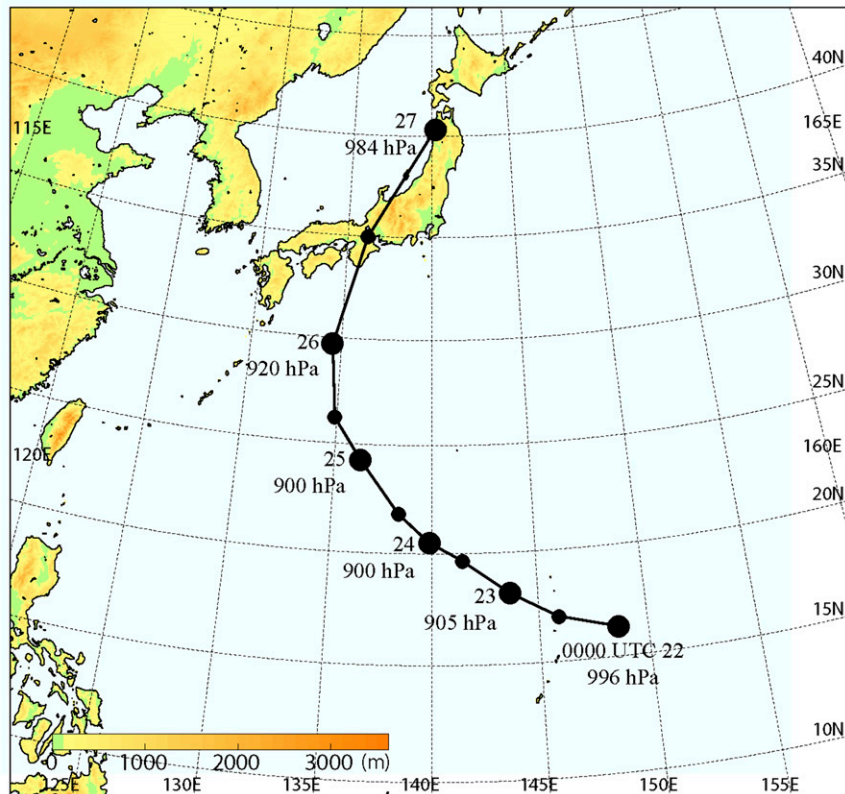
Fig. 1. The JMANHM simulation domain showing the track of Typhoon Vera (1959) at 12-h intervals (large dots, 0000 UTC; small dots, 1200 UTC). Large dots are labeled with the day in September 1959 and the central pressure at that location.

et al. 2015) dataset with a spatial resolution of $1.25° \times 1.25°$. All simulations started at 0000 UTC 22 September 1959 and were integrated over at least 5 days. The computational domain of JMANHM was $4500\,km \times 4200\,km$ (Fig. 1), and the domains of other models were set to cover approximately the same region (not shown).

To obtain the initial and boundary conditions for the global warming climate, we used the results of climate runs by the JMA atmospheric GCM (AGCM) with a horizontal resolution of 20 km (AGCM20; Mizuta et al. 2012; Murakami et al. 2012). A present-day climate run for the period 1979–2003 and four future climate runs for the period 2075–99 were conducted with AGCM20. The future climate runs were driven by four different SST change patterns projected by models from phase 5 of the Coupled Model Intercomparison Project (CMIP5) under the RCP8.5 scenario (Mizuta et al. 2014): the CMIP5 multimodel ensemble mean (PWMM) and three SST distribution clusters (PWC1, PWC2, and PWC3). Because Typhoon Vera occurred in September, future changes in the September monthly mean for SST, atmospheric temperature, and water vapor were added to the initial and boundary conditions of the CNTL simulation. All

increments include horizontal variability. The change in relative humidity was not considered because recent studies have indicated little change in tropospheric relative humidity between the present-day and future climates (e.g., Knutson and Tuleya 2004; Takemi et al. 2012). Following Ito et al. (2016), the future climate conditions are referred to as PW conditions. Thus, we used four sets of PW conditions for four global warming climate simulations. Several sensitivity experiments were conducted with JMANHM: the CNTL simulations without the spectral nudging scheme (noSN experiment) and that started from 0000 UTC 21 September 1959 (2100 experiment). We also conducted the PWMM simulation by JMANHM with water vapor increments (QV experiment) and wind increments (UV experiment) to study the impacts of the change in relative humidity and vertical wind shear (e.g., Gray 1968; Reasor et al. 2013).

3. Environmental conditions for the current climate and the future, warmer climate

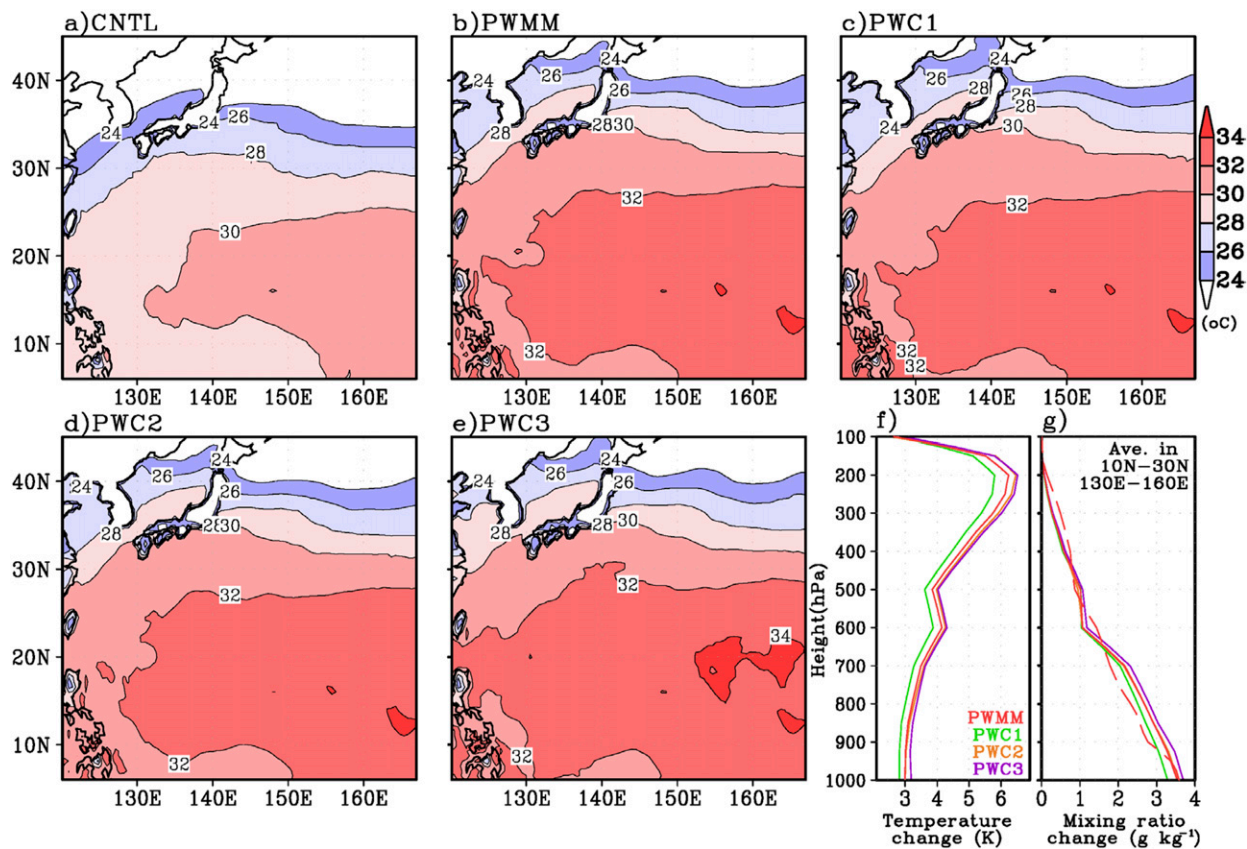The initial conditions used for the current and future climate simulations are shown in Fig. 2. At

FIG. 2. Horizontal distributions of sea surface temperature in the (a) CNTL, (b) PWMM, (c) PWC1, (d) PWC2, and (e) PWC3 simulations. Mean profiles of changes in (f) temperature and (g) the water vapor mixing ratio in 10°–30°N, 130°–160°E in the PWMM (red), PWC1 (green), PWC2 (orange), and PWC3 (purple) simulations, compared with the CNTL simulation values. A red dashed line in (g) indicates the change for the QV-increment simulation.

0000 UTC 22 September 1959, Typhoon Vera was at around 16.5°N, 148.5°E and traveling northwestward, according to the JMA Regional Specialized Meteorological Center (RSMC) best-track dataset (Fig. 1). In that region, SST was higher than 30°C at that time, indicating that sea conditions around the typhoon were favorable for intense TC development (e.g., DeMaria and Kaplan 1994). In the future climate, SST increases 2°–3° to the south of the Japanese islands, and regions with SST higher than 30°C extend to western Japan. Meanwhile, mean profiles of air temperature changes in 10°–30°N, 130°–160°E show warming throughout the troposphere that is maximized in the upper troposphere (Fig. 2f). This increase of the temperature change with height indicates a stabilization of atmospheric conditions. Therefore, the future changes in environmental conditions could have both positive and negative effects on TC development, consistent with the findings of previous studies (e.g., Hill and Lackmann 2011; Knutson and Tuleya 2004; Shen et al. 2000). Water vapor also

increases in response to warming. In the future climate, the temperature increase in the lower troposphere is approximately 3 K, and the water vapor mixing ratio increase in the lower troposphere is approximately 3.5 g kg^{-1}.

To estimate the maximum TC intensity changes due to the changes in the atmospheric environment and SST, we used the Emanuel (2006) model to calculate maximum potential intensity (E-MPI) from the atmospheric conditions (pressure, temperature, and water vapor mixing ratio) and SST in the vicinity of the typhoon at 0000 UTC 22 September 1959. E-MPI in the current climate simulation was 862 hPa in terms of minimum central pressure and 84 m s^{-1} in terms of the maximum 10-m wind speed (Table 2). In the future climate, E-MPI in terms of minimum central pressure (maximum 10-m wind speed) decreased (increased) by 17–18 hPa (5–6 m s^{-1}). Therefore, despite the stabilization of atmospheric conditions, all environmental changes in the future climate lead to an increase in the maximum intensity of the future TC.

TABLE 2. Minimum central pressures in JRA-55, the RSMC best-track data, CNTL simulations, and the ensemble mean of the PW simulations (PW_Av); dCP is the difference between the CNTL and the PW ensemble mean values for each model.

	JRA-55	BT	CReSS	JMANHM	MM5	WRF	WRFB	MPI
CNTL	922	895	916	907	905	928	901	862
PW_Av	—	—	894	884	868	909	892	844
dCP	—	—	22	23	37	19	9	18

4. Results of the multimodel ensemble simulations

a. Intensity changes of simulated typhoons

The multimodel ensemble experiment results, including those in the sensitivity experiments, all showed robustly that the maximum intensity of the typhoon is increased under future PW conditions (Table 2 and Fig. 3). All future typhoons decrease the minimum central pressures, regardless of the model physics and the boundary conditions. The ensemble-mean decreases in the minimum central pressure in each model, except WRFB, ranged between 19 and 37 hPa. The simulated minimum central pressure decreases are slightly larger than the E-MPI of 18 hPa. Most models except CReSS simulated almost the same tracks as the RSMC best-track data (not shown).

Figure 4 compared the temporal evolution of central pressure, maximum azimuthal mean tangential wind speed at an altitude of 10 m Vtmax and the radius of Vtmax RMW$_{10m}$ between the CNTL and PW simulations. According to the RSMC best-track data, Typhoon Vera intensified rapidly and attained a minimum central pressure of 895 hPa at 0600 UTC 23 September 1959. Subsequently, the typhoon's intensity weakened once

to a central pressure of 905 hPa but then intensified again to a central pressure of 900 hPa at 0000 UTC 25 September. JRA-55 did not capture the evolution of Typhoon Vera from 1200 UTC 23 September to 1200 UTC 24 September, and the CNTL storms in all models followed JRA-55 because the initial vortex was provided by JRA-55. The impact of the initial vortex on the TC simulation is discussed in section 5 by the results of the WRFB simulations.

Although all models underestimated the first intensity peak of Typhoon Vera at the beginning of the integration time, JMANHM and MM5 successfully simulated CNTL storms that developed into intense typhoons with the minimum central pressures lower than 910 hPa. Both models indicated that not only the maximum intensity but also the intensification rate of the typhoon in the future climate would increase while RMW$_{10m}$ decreased rapidly (Fig. 4). For example, the CNTL and PW storms simulated by JMANHM developed at similar rates from the beginning of the integration time until 1200 UTC 24 September 1959. Then, all PW storms started to intensify at high rates, a decrease in central pressure more than −10.5 hPa in a 6-h period, meeting the rapid intensification (RI)
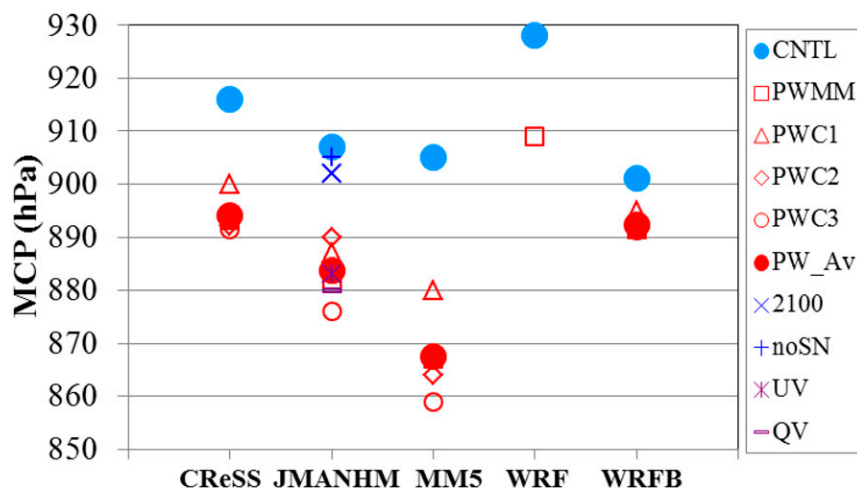

FIG. 3. Minimum central pressures in the CNTL (cyan) and PW (red) simulations by CReSS, JMANHM, MM5, WRF, and WRFB. Red dots indicate the ensemble mean of the PW simulations. Results of the sensitivity experiments by JMANHM are shown by blue (CNTL) and purple (PW) crosses, respectively.
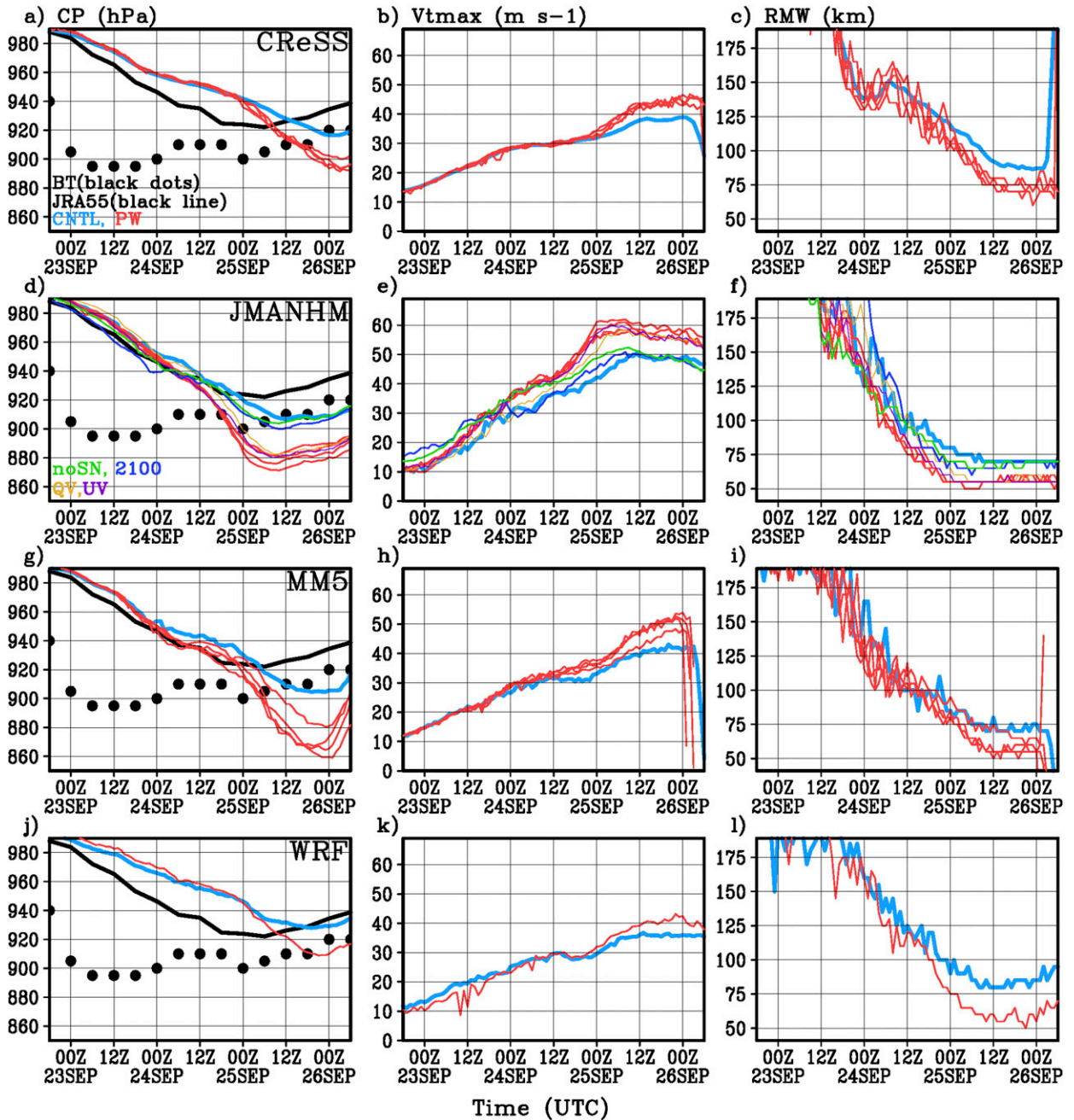
FIG. 4. Temporal evolution of (a) central pressure (CP), (b) maximum azimuthally averaged tangential wind at 10-m altitude (Vtmax), and (c) radius of Vtmax (RMW) in simulations by CReSS. The black dots and black line in (a) indicate the central pressure in the RSMC best-track data and JRA-55, respectively. Cyan and red lines indicate values for the CNTL and the four PW simulations, respectively. (d)–(f) As in (a)–(c), but for simulations by JMANHM. (g)–(i) As in (a)–(c), but for simulations by MM5. (j)–(l) As in (a)–(c), but for simulations by WRF. Green (noSN), blue (2100), orange (QV), and purple (UV) lines in (d)–(f) indicate the results of sensitivity experiments.

criterion, which is defined as a decrease in central pressure of at least 42 hPa in a 24-h period (Holliday and Thompson 1979). The PW storms simulated by MM5 also intensified rapidly after 2100 UTC 24 September 1959 while RMW_{10m} rapidly decreased. As a result, RMW_{10m} was smaller in all storms in the PW simulations than it was in the CNTL simulations, regardless of the model physics.

b. Structural changes of the inner core during the mature phase

We first focus on the inner-core structures of the simulated typhoons during the mature phase, defined by the 6 h prior to the time that the minimum central pressure was reached. The major structural changes in the inner core during the mature phase appeared within a radius of 100 km according to the 6-h mean radial profiles of sea level pressure, hourly precipitation, and tangential wind speed at an altitude of 10 m (Vt_{10m}) (Fig. 5). The peak values and radial changes of hourly precipitation and Vt_{10m} within RMW_{10m}, which were very large in the PW simulations, indicate that sudden changes occur in precipitation and winds around the storm center. Inward shifts of the peaks indicate contraction of the eye and of RMW_{10m}.

The inner-core structure is closely related to the eyewall updrafts. Figure 6 shows eyewall updrafts, defined by the azimuthally averaged vertical velocity, during the mature phase. There were, indeed, several significant differences in intensity, radial location, and the shape of the eyewall updraft among the models. However, it is evident that all future PW storms exhibited taller and more intense eyewall updrafts, compared with the CNTL storms. The regions with eyewall updrafts stronger than $0.2 \, \text{m s}^{-1}$ exceeded at an altitude of 17 km in all the future simulations. In addition, the radial locations of eyewall updrafts were smaller in all the future simulations than in the current simulations, which were consistent with contractions of the eye and RMW_{10m}.

c. Structural changes of the inner core during the period with a high intensification rate

To understand the processes through which a PW storm intensifies rapidly as contracting the RMW, we explored the inner-core structures during the period of rapid intensification. We selected the PWMM simulation by JMANHM as a typical PW case because the CNTL storm simulated by JMANHM developed into an intense typhoon with a minimum central pressure lower than 910 hPa and best reproduced the maximum intensity location of Typhoon Vera (not shown).

The PWMM storm exhibited typical changes compared with the CNTL storm (Fig. 7), namely, a higher intensification rate during the RI phase and a smaller RMW_{10m} during the mature phase. The maximum intensification rate of the PWMM storm was more than doubled that of the CNTL storm (Fig. 7b). Although the PWMM storm intensified at a higher rate and its maximum intensity was increased compared with that of the CNTL storm, changes in the near-surface structures of both storms appeared within a radius of 100 km

(Figs. 5d–f). Indeed, there was not much difference in the location of the 980-hPa contour between the CNTL and PWMM storms (Figs. 7d,e), although the eye of the PWMM storm was much smaller than that of the CNTL storm.

On the basis of the intensification rate, the intensification period was divided into two phases: a gradual intensification phase (phase I) and an RI phase (phase II). Phase I was defined as the period before phase II with a decrease in central pressure less than $-10.5 \, \text{hPa}$ in a 6-h period, and phase II was defined as the period with a decrease in central pressure more than $-10.5 \, \text{hPa}$. In addition, the period during which the 6-h mean central pressure of the PWMM storm was equal to that of the mature CNTL storm was defined as period A. Phase I, phase II, and period A of the PWMM storm are indicated in Fig. 7a.

Figure 8 compares mean radial–height cross sections of vertical wind velocity, radial wind velocity Vr, and the water vapor mixing ratio in the PWMM storm during period A with those in the CNTL storm during the mature phase. The mean minimum central pressure and RMW_{10m} of the CNTL storm during the mature phase and those of the PWMM storm during period A were equivalent (Fig. 7). Following Rogers et al. (2013), the radial axis in Fig. 8 is normalized by the radius of maximum wind speed at an altitude of 2 km RMW_{2km}.

Although there were no significant differences in storm intensity, the eyewall updraft of the PWMM storm during period A was already considerably taller and stronger than that of the mature CNTL storm (Figs. 8a,b). The regions with a vertical velocity increase more than $1 \, \text{m s}^{-1}$ show increases in the updraft in the mid-to-upper troposphere around RMW_{2km} and in the lower-to-midtroposphere inside RMW_{2km} in the PWMM simulation (Fig. 8c).

The upper-tropospheric outflows in the PWMM storm were stronger and appeared at higher altitudes than those in the CNTL storm (Figs. 8d–f). Below the upper-tropospheric outflow between altitudes of 5 and 10 km, regions with inflow smaller than $-1 \, \text{m s}^{-1}$ appeared outside RMW_{2km} in the PWMM storm. The inward transport of absolute angular momentum (AAM) is associated with a midtropospheric inflow below the upper-tropospheric outflows (not shown). According to Fudeyasu and Wang (2011), midtropospheric inflow is induced by diabatic heating in upper-tropospheric anvil clouds and transports AAM inward, causing the circulation outside the eyewall to spin up. There was little difference, however, in the near-surface inflow between the mature CNTL storm and the PWMM storm during period A.

Despite the lack of a large difference between the near-surface inflows, the eyewall updraft of the PWMM storm could obtain a large amount of water vapor
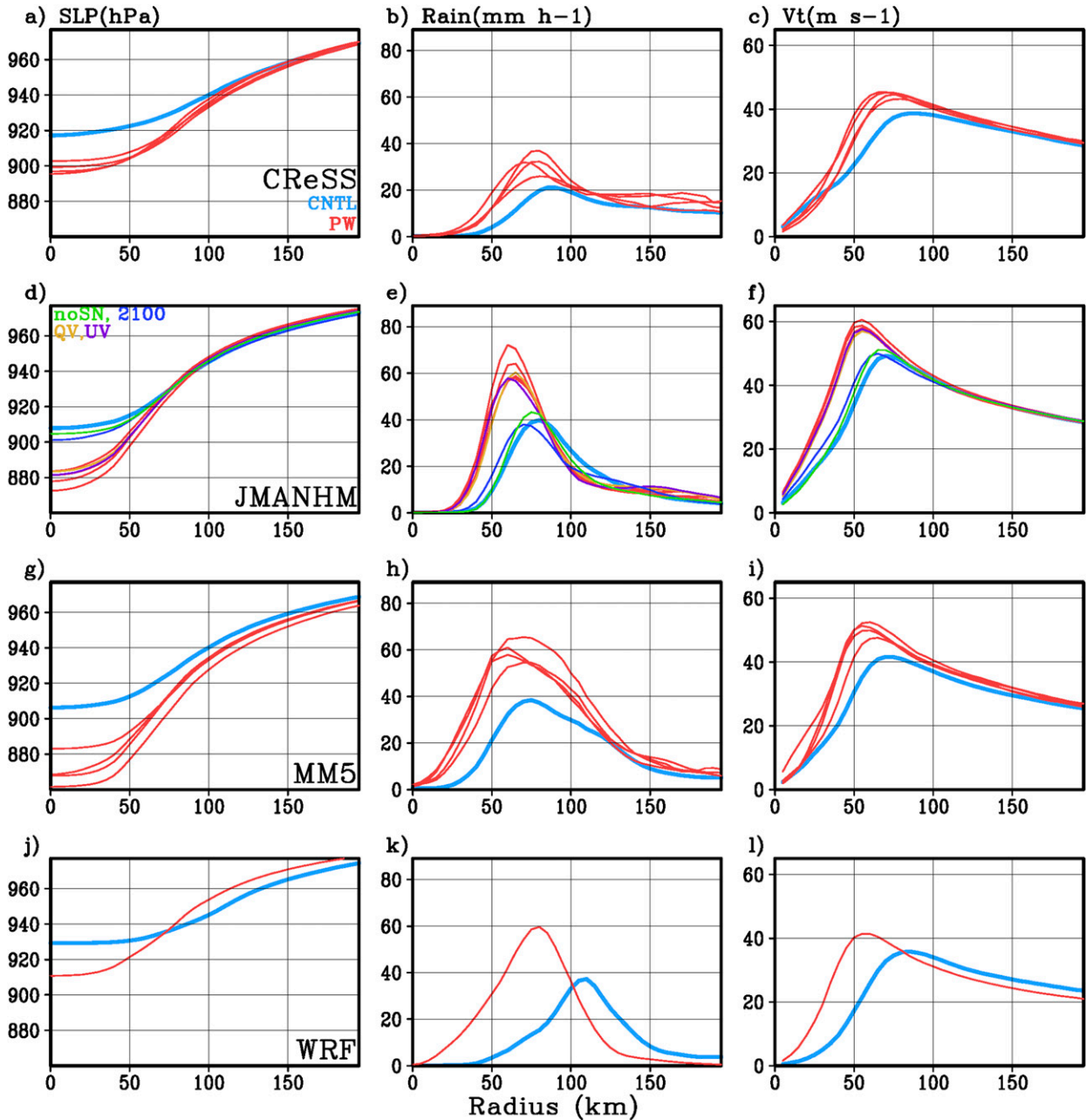
FIG. 5. Storm-centered composite radial profiles of 6-h mean azimuth-averaged (a) sea level pressure (SLP), (b) hourly precipitation (RAIN), and (c) tangential wind speed at 10-m altitude (Vt) during the mature phase in the CNTL (cyan) and PW (red) simulations by CReSS. (d)–(f) As in (a)–(c), but for JMANHM. (g)–(i) As in (a)–(c), but for MM5. (j)–(l) As in (a)–(c), but for WRF. Green (noSN), blue (2100), orange (QV), and purple (UV) lines in (d)–(f) indicate the results of sensitivity experiments.

because the amount of water vapor in the lower tropo-sphere was substantially increased compared with the CNTL storm (Figs. 8g–i); in fact, the water vapor mixing ratio in the inflow boundary layer (IBL) of the PWMM storm was greater than that in the IBL of the CNTL storm by more than $4 \, \mathrm{g \, kg^{-1}}$. In addition, the presence of regions with a water vapor increase larger than $3 \, \mathrm{g \, kg^{-1}}$

inside the eyewall updraft suggests that the upward transport of water vapor by the intense eyewall updrafts was increased in the PWMM storm. Warming by the latent heat (LH) release of condensation would enhance upward buoyancy in the updrafts. Thus, the secondary circulation above the IBL would be intensified in the future climate simulation.
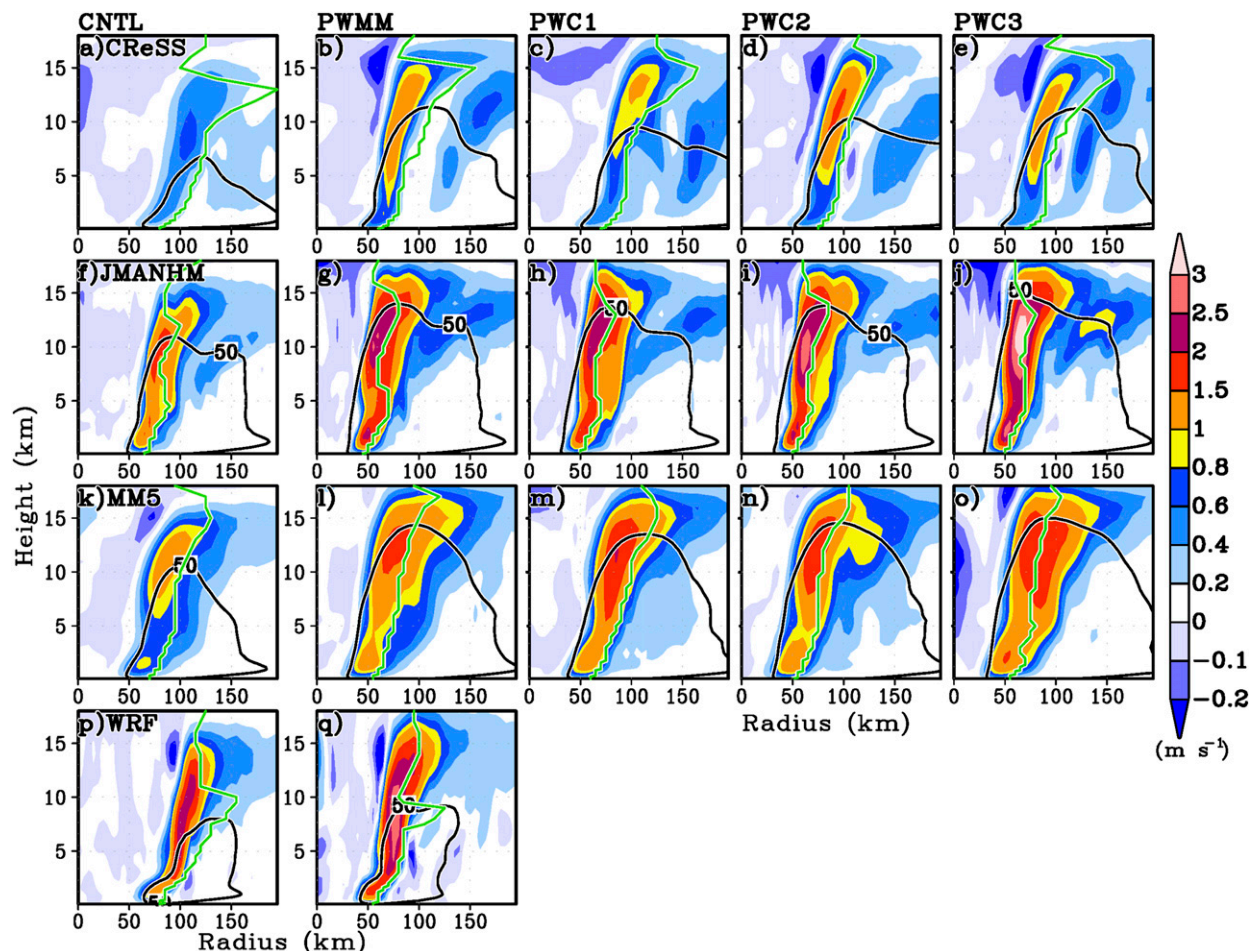
FIG. 6. Six-hour azimuth-averaged radial–vertical cross sections of vertical velocity during the mature phase in the (a) CNTL, (b) PWMM, (c) PWC1, (d) PWC2, and (e) PWC3 simulations by CReSS. (f)–(j) As in (a)–(e), but for JMANHM. (k)–(o) As in (a)–(e), but for MM5. (p),(q) As in (a)–(e), but for WRF. Thick black lines indicate azimuth-averaged tangential wind velocity (Vt) of 50 m s⁻¹, and thick green lines indicate the Vt axis defined by the radius of maximum Vt at each altitude.

The PWMM storm underwent extreme RI from 1200 UTC 24 September to 0300 UTC 25 September 1959. Mean changes in the inner-core structure during those 18 h (phase II) in the PWMM simulation by JMANHM are shown in Fig. 9. The vertical velocity change indicates that the eyewall updraft intensified inside the RMW_{2km} during phase II (Fig. 9a), whereas the regions showing a negative vertical velocity change outside RMW_{2km} imply contraction of the eyewall updraft region. The region of increased updrafts inside RMW_{2km} corresponds well to the region of increased water vapor (Fig. 9b), which indicates that the upward water vapor flux increased in the intensifying updraft inside RMW_{2km}. In addition, the total solid water (graupel, snow, and ice) mixing ratio also increased in the moist and intense eyewall updraft, suggesting that a large amount of latent heat was released inside the RMW_{2km} (Fig. 9c).

According to previous modeling studies, the efficiency with which diabatic heating drives increases in the maximum winds of the vortex depends on the radial location of the heating relative to the RMW; heating inside the RMW is more efficient than heating outside the RMW (e.g., Hack and Schubert 1986; Pendergrass and Willoughby 2009; Vigh and Schubert 2009). In addition, abundant transport of water vapor moistened the deep layers in the vicinity of the eyewall updraft, and this deep-layer moistening is an essential condition for a high intensification rate (e.g., Nolan 2007). Similar results to those shown in Fig. 9 were found in the PW simulations by the other models during phase II (not shown).

d. Evolution and near-surface water vapor of the simulated typhoons

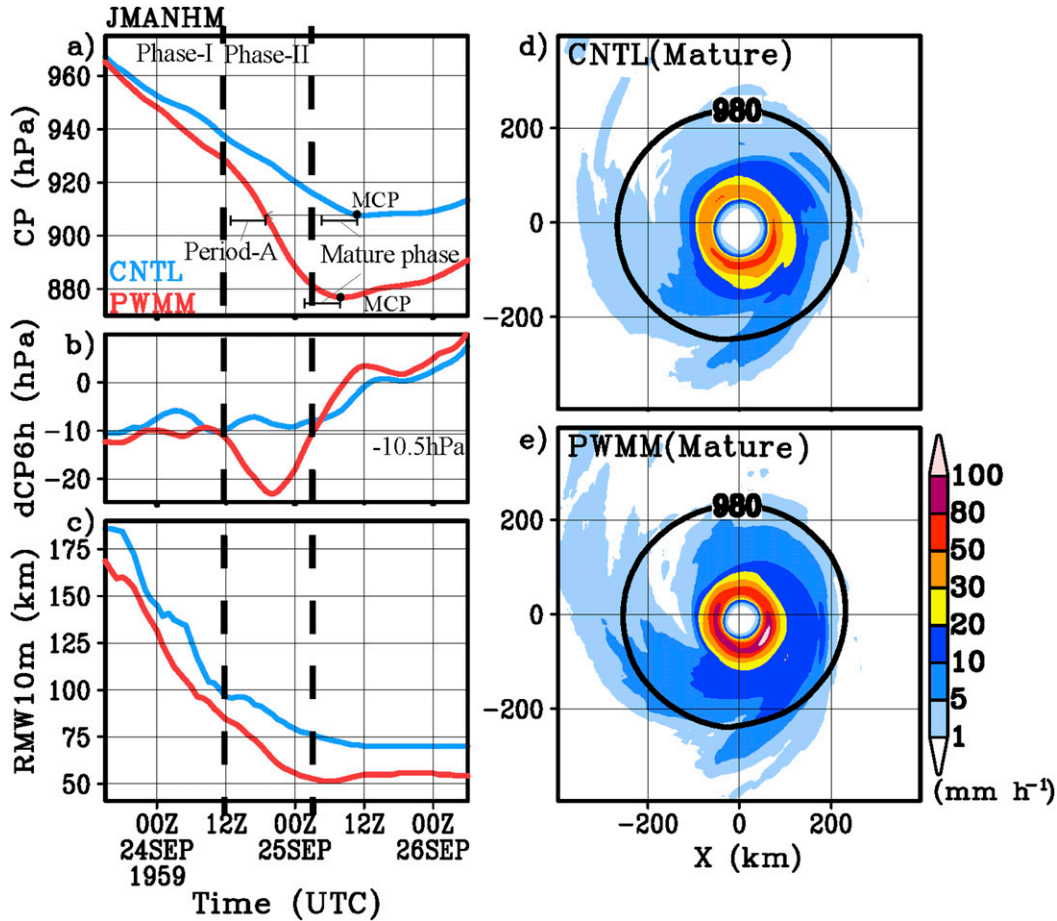The results presented in section 4c indicate that an increase in the amount of lower-tropospheric water

FIG. 7. Six-hour moving average temporal evolution of (a) CP, (b) 6-h changes in central pressure (dCP6h), and (c) radius of Vt_{max} (RMW_{10m}) in the CNTL (cyan) and PWMM (red) simulations by JMANHM. Horizontal distributions of 6-h mean precipitation for (d) the CNTL storm and (e) the PWMM storm during the mature phase. The thick black contour in (d) and (e) indicates a mean sea level pressure of 980 hPa.

vapor plays a key role in increasing the intensification rate during RI. Therefore, we examined the temporal evolution of lower-tropospheric water vapor in the eyewall region in the CReSS, JMANHM, and MM5 simulations (Fig. 10). We defined lower-tropospheric water vapor in the eyewall region as the mean water vapor mixing ratio between normalized radii of 0.7 and 1.3 averaged over the lowest 500 m (see Fig. 8).

During phase I, a simulated typhoon gradually intensified as the RMW_{10m} decreased (Fig. 4). After the RMW_{10m} had contracted to less than 150 km, the lower-tropospheric water vapor in the eyewall region increased gradually, and then the storm initiated RI. It is notable that the mean water vapor mixing ratio in the PW storms was quite large in all models, increasing over that in the CNTL storm by 3–4 g kg^{-1}.

The increases in lower-tropospheric water vapor should be closely related to the sensible and latent heat

fluxes beneath the inner core. Despite future changes in the mean sensible heat (SH) flux within a radius of 200 km being relatively small in all models (Figs. 10d–f), the mean latent heat flux significantly increased from the CNTL to the PW simulations (Figs. 10g–i). Enthalpy fluxes in the vicinity of eyewall updrafts are key factors in TC development (Xu and Wang 2010). According to Miyamoto and Takemi (2013), RI initiates when low-level parcels obtain high enthalpy from the underlying ocean. In the present study, most of the PW storms simulated by JMANHM and MM5 initiated RI when the lower-tropospheric water vapor beneath the eyewall updrafts was maximized. This finding suggests that the enhancement of intensification rates during RI in the future climate is attributable to an abundant supply of water vapor to the lower troposphere from the warmer sea. In fact, the models that simulated intense typhoons (JMANHM and MM5) showed a relatively large latent
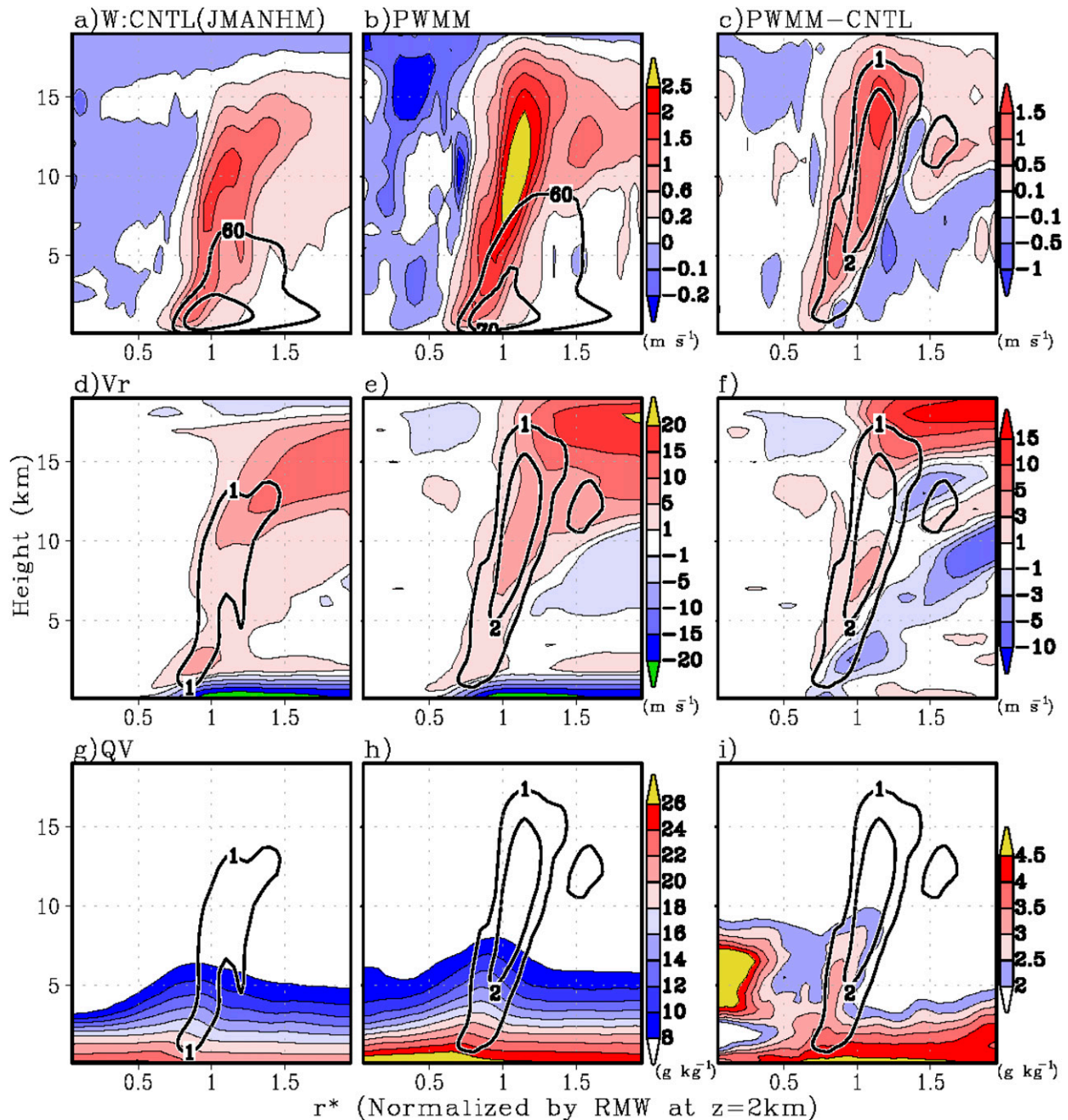
FIG. 8. Six-hour azimuth-averaged radial–vertical cross sections of vertical velocity w in the (a) CNTL simulation during the mature phase and (b) PWMM simulation during period A by JMANHM; (c) PWMM minus CNTL. (d)–(f) As in (a)–(c), but for Vr. (g)–(i) As in (d)–(f), but for the water vapor mixing ratio (QV). Black contours in (a) and (b) indicate Vt (60 and 70 m s^{-1}), and those in (c)–(i) indicate vertical velocity (1 and 2 m s^{-1}). The x-axis quantity r^* indicates radius normalized by the RMW at an altitude of 2 km.

heat flux, whereas the intensity of typhoons simulated by the model showing a relatively small latent heat flux (CReSS) was relatively weak.

Thus, the remaining question to be solved is why the future storms could not initiate RI earlier, while the lower-tropospheric water vapor was much larger than

the values when the CNTL storms initiated RI. The previous studies indicate that inertial stability (IS) inside the RMW is closely related to the RI because an increase of inertial stability prevents air parcels from being displaced outward in the radial direction and allows for a more efficient dynamic response to imposed
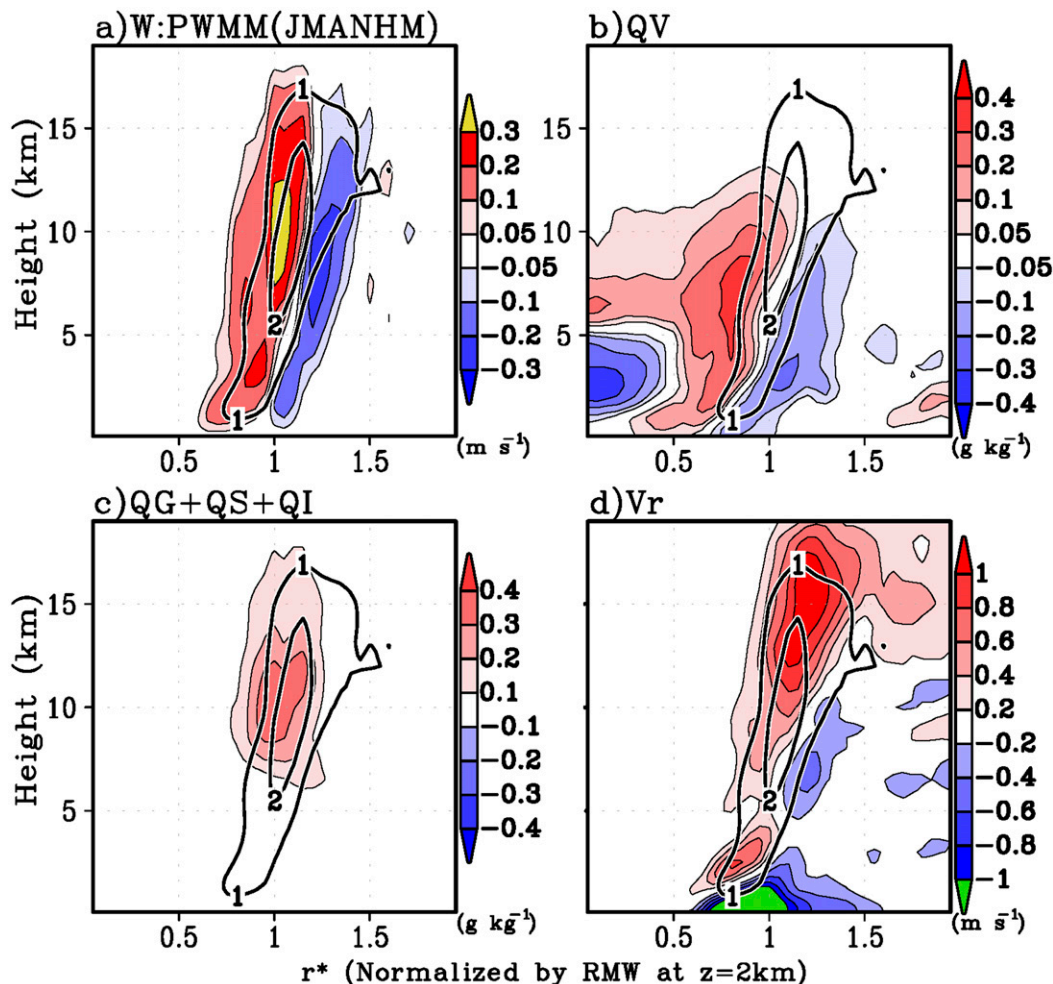
FIG. 9. Mean azimuth-averaged radial–vertical cross sections of changes in (a) vertical velocity (i.e., w; m s^{-1} h^{-1}); (b) the water vapor mixing ratio (QV; g kg^{-1} h^{-1}); (c) the sum of the graupel, snow, and ice mixing ratios (QG + QS + QI; g kg^{-1} h^{-1}); and (d) Vr (m s^{-1} h^{-1}) during phase II in the PWMM simulation by JMANHM. Black contours show the mean updraft (1 and 2 m s^{-1}); the $r*$ is as in Fig. 8.

sources of convective heating inside the RMW (Hack and Schubert 1986; Pendergrass and Willoughby 2009; Vigh and Schubert 2009). The temporal evolutions of mean inertial stability below an altitude of 10 km inside RMW$_{2km}$ are shown in Figs. 10j–l. The initial vortex given by JRA-55 was weak so that the inertial stability was low at the beginning of integration time. As the RMW contracted, the inertial stability around the storm center increased gradually through vortex axisymmetrization. There were no large differences in the inertial stability values between the CNTL and PW storms during the period. However, around the time when the values increased by 0.5×10^{-6} s^{-2}, the PW storms started to intensify at higher rates than the CNTL storm. After the onset of RI, the simulated storms with larger amounts of the lower-tropospheric water vapor intensify

at higher rates (Fig. 11). The 12-h changes in central pressure and mean lower-tropospheric water vapor in all the simulations show a high correlation coefficient value of -0.81.

5. Discussion

a. How does climate change affect the TC intensification process?

All future typhoons simulated by the four different models showed increased maximum intensity compared with that in the current climate. Furthermore, all models indicated that not only the maximum intensity but also the intensification rate of the typhoon in the future climate would increase while RMW$_{10m}$ decreased rapidly (Fig. 4).
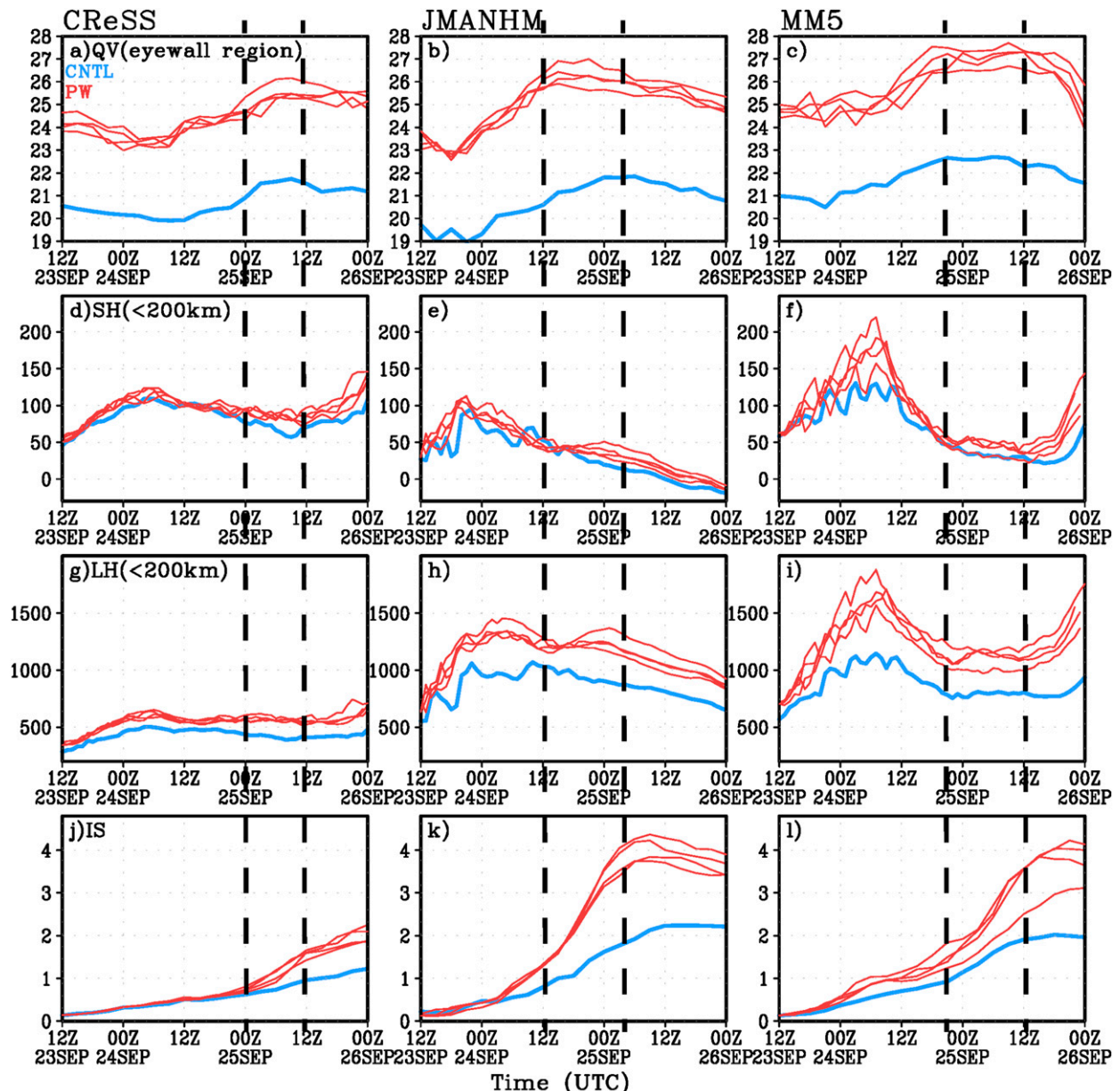
FIG. 10. Temporal evolution of mean lower-tropospheric water vapor (QV; g kg^{-1}) in the eyewall region in the CNTL (cyan) and PW (red) simulations by (a) CReSS, (b) JMANHM, and (c) MM5. The eyewall region was defined as $0.7 \leq r* \leq 1.3$. (d)–(f) As in (a)–(c), but for mean SH (W m^{-2}) within a radius of 200 km. (g)–(i) As in (d)–(f), but for LH (W m^{-2}). (j)–(l) As in (d)–(f), but for mean squared IS (10^{-6} s^{-2}) below an altitude of 10 km inside the radius of maximum wind speed at an altitude of 2 km. Black dashed vertical lines indicate the beginning and end of phase II in the PWMM simulations by each model.

A schematic diagram of the intensification process of a future intense TC is shown in Fig. 12. At the beginning of the integration time, the simulated TC intensifies gradually as the RMW contracts (phase I in Fig. 7). The results of all four models indicated that there was little difference in the temporal evolution of simulated typhoons between the current and future climates during phase I (Fig. 4). The impact of future,

warmer climate conditions appeared during the RI phase when the intensification rate increased greatly. In the future climate, SST to the south of the Japanese islands is projected to increase by 3°C (Fig. 2), and a warmer sea provides more water vapor to the lower troposphere (Fig. 10). The abundant water vapor was supplied to tall and intense eyewall updrafts, which formed continuously inside the RMW (Figs. 8 and 9),
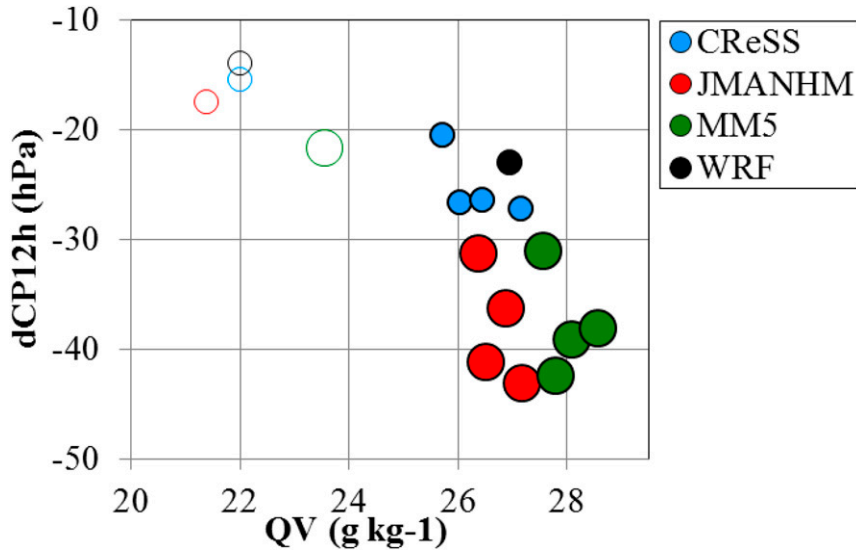
FIG. 11. Scatter diagram of mean lower-tropospheric water vapor (QV; g kg^{-1}) in the eyewall region at the beginning of phase II and the 12-h changes in central pressure (dCP12h) from the beginning of phase II in the CNTL (open circles) and PW (filled circles) simulations by CReSS (blue), JMANHM (red), MM5 (green), and WRF (black). Large (small) circles indicate that the mean squared inertial stability (IS in Fig. 10) at the beginning of phase II was higher (lower) than 1.0×10^{-6} s^{-2}.

and contributed to rapid formation of condensed water in the updrafts (Fig. 9).

A study of intensification processes before and after the onset of RI has revealed that a clear difference in diabatic heating associated with the eyewall updraft appears in the inner core from before to after the onset (Miyamoto and Takemi 2015): a high diabatic heating region occurs around the RMW after the TC initiates RI. On the basis of their results, Miyamoto and Takemi (2015) suggested a positive feedback process operated
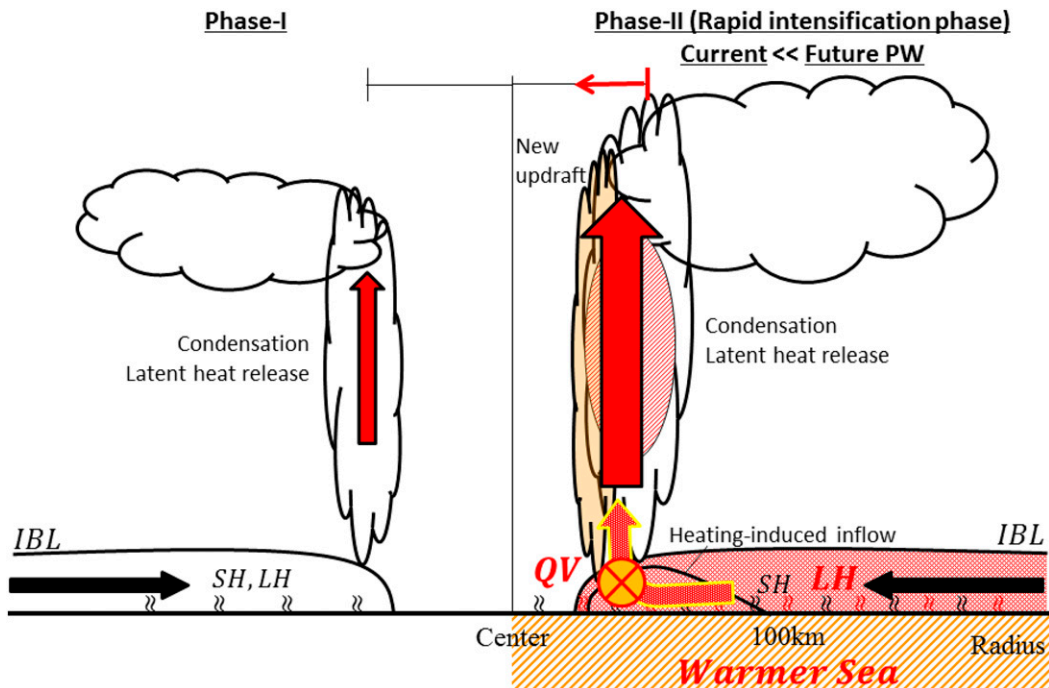

FIG. 12. Schematic diagrams of the intensification process during phases I and II.

during RI between the secondary circulation and diabatic heating in the eyewall (e.g., Charney and Eliassen 1964; Ooyama 1969). In fact, our study showed a large increase in the total solid water mixing ratio around and inside the RMW during phase II. Furthermore, the increase in near-surface inflow only around the eyewall region (Fig. 9d), a pattern similar to that in Vr induced by heating shown by Stern et al. (2015), also suggests the enhancements of heating-induced near-surface inflow and hence horizontal wind speed in the vicinity of the eyewall in the future climate. Thus, the RI process in the future simulations is enhanced by the release of latent heat associated with a rapid increase in the solid water mixing ratio caused by a large increase in near-surface water vapor derived from the future, warmer sea.

Model surface parameters have large impacts on the enthalpy fluxes from the sea surface, which are crucial for TC development (e.g., Emanuel 1986; Rotunno and Emanuel 1987). Indeed, CReSS, which considered the ocean cooling effect by the 1D-slab ocean model, simulated relatively weak storms. The IBL structures determined by the PBL scheme control the water vapor supply to the eyewall updraft in simulations (e.g., Kanada et al. 2013; Rotunno and Bryan 2012). In addition, microphysics processes affect the amount and location of diabatic heating (e.g., McFarquhar et al. 2012; Zhu et al. 2015). Nonetheless, the most important findings in the present study are that all four models, despite their having different schemes, project the same results: an intense TC will intensify more rapidly and become more intense under future, warmer climate conditions. This result does not depend on whether the model considers the ocean effect. Thus, the results of multimodel ensemble experiments strongly support the robustness of the changes in intense TCs in the future climate shown in the present study.

b. Impact of the initial TC vortex

All four 5-km-mesh models underestimated the rate of intensification from 1200 UTC 23 September to 1200 UTC 24 September 1959 for Typhoon Vera (Fig. 4). This underestimation was due to the initial vortex structure provided by JRA-55. The three-dimensional structure of the simulated TCs depends considerably on the model resolution (e.g., Bengtsson et al. 2007; Gentry and Lackmann 2010; Roberts et al. 2015; Kanada and Wada 2016), and the horizontal resolution of the initial atmospheric data of JRA-55, $1.25° \times 1.25°$, is too coarse to represent the three-dimensional typhoon vortex structure. To simulate the evolution of an intense TC by a nonhydrostatic model, the initial vortex is crucial because an axisymmetric inner-core structure is essential to produce a high intensification rate (e.g., Alvey et al. 2015; Kieper and Jiang 2012; Rogers et al. 2013). The inertial stability increases through vortex axisymmetrization. In fact, mean inertial stability inside the RMW was considerably low in the beginning of integration time. The values increased gradually for 2–3 days and then the storms initiated the RI (Fig. 10).

Various initialization methods have been developed to improve initial conditions in TC simulations, including vortex relocation (e.g., Hsiao et al. 2010) and dynamical initialization (e.g., Cha and Wang 2013) schemes. The vortex relocation scheme, which is a TC bogus scheme, inserts a synthetic Rankin vortex in the initial conditions (e.g., Leslie and Holland 1995; Ueno 1989).

To study the impact of the initial vortex on simulations of Typhoon Vera, we conducted sensitivity experiments for the CNTL and PW simulations by using WRF both with (WRFB) and without (WRF) the TC bogus scheme (Fig. 13). The initial bogus vortex was set to have the maximum wind speed of $50 \, \text{m s}^{-1}$ and the radius of the maximum wind of 50 km, with the same wind speed being set in the depth from the surface to the 600-hPa level, but the wind speed exponentially decreased above the 600-hPa level to the 100-hPa level. The same initial vortex was imposed both for the CNTL and PW simulations. The choice of this intensity was intended to reproduce the rapid intensification and the maximum intensity of Vera in the September 1959 condition. The discussion on the use of the TC bogus scheme can be found in Takemi et al. (2016).

The CNTL storm simulated by WRFB apparently captured the temporal evolution of central pressure (Fig. 13a) but not the evolutions of Vt_{max} and RMW_{10m}. In general, the maximum wind speed of a TC increases and its central pressure decreases as the RMW contracts (e.g., Miyamoto and Takemi 2013). In all WRFB simulations, however, the initial RMW_{10m} increased with time as Vt_{max} decreased.

The reason why the response to the warming in the simulations with the TC bogus scheme is different from that in the simulations without the TC bogus is due to the different temporal evolution of the size of the TC core as shown in terms of the RMW. Without the TC bogus scheme the contraction of the TC core can be seen (see Fig. 4l), while with the TC bogus such a contraction of the size of the TC core is not seen (Fig. 13c). In addition, the difference in the RMW between the CNTL and PW simulations is much smaller in the simulations with the TC bogus scheme than without the TC bogus. Similar TC core sizes between the CNTL and PW simulations with the TC bogus scheme led to the smaller difference in the warming impact on Vera's intensity in the simulations with the TC bogus than without the TC bogus.

The results of the sensitivity experiments showed that the TC evolution in a simulation is highly sensitive to the initial vortex. Indeed, a number of studies have shown that a TC bogus scheme can reasonably reproduce TC features with improved track and intensity (e.g., Knutson
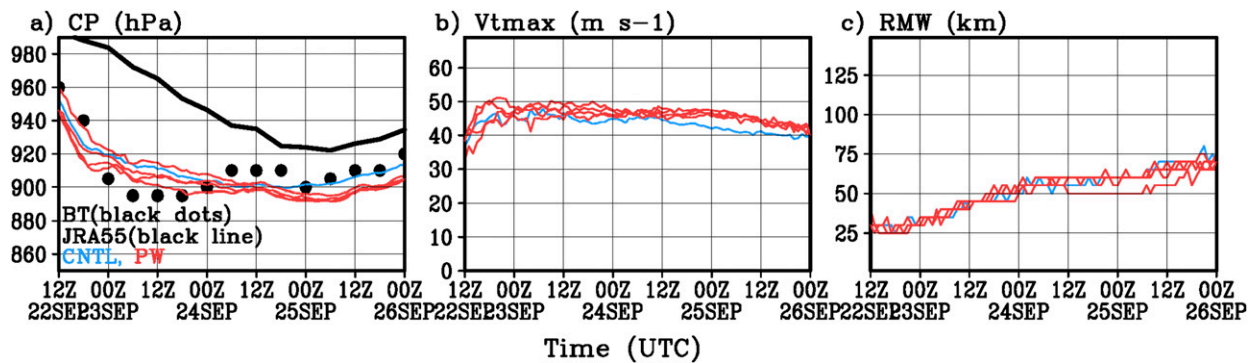
FIG. 13. As in Fig. 4, but for WRFB.

and Tuleya 1999). However, our results also imply that great care is needed when choosing the characteristics of the bogus vortex. We can evaluate the results of CNTL simulations by using best-track datasets. However, in PW simulations, considerable uncertainties remain in the initial vortex because we have no references for the initial vortex in the future climate. Use of advanced initialization methods such as a dynamical initialization scheme (e.g., Cha and Wang 2013) and piecewise potential vorticity inversion (Davis 1992) will help to produce better simulations and forecasts of TC evolution.

c. Other future intense TCs

In the present study, all CNTL and PW simulations used the same initial vortex. Therefore, the results shown represent the changes that can be expected in intensity and inner-core structure of a Typhoon Vera–like vortex in the future climate. This raises the question of whether the future changes found in this study are robust for other intense TCs.

Recently, Kanada et al. (2013) used a 2-km-mesh nonhydrostatic model to examine the effects of global warming on the structure of intense TCs. They chose 6 of the top 10 TCs in global warming projections calculated by AGCM20 (Murakami et al. 2012) for the present-day and future climates and conducted dynamical downscaling experiments. In fact, their comparison between present-day and future intense TCs showed structural changes of the inner core in the future climate similar to those shown in the present study (Fig. 5): relatively tall and intense eyewall updrafts and decreases in the eye diameter and RMW were accompanied by increases in precipitation and near-surface wind speeds within a radius of 100 km.

The cause of high intensification rates in future TCs is an increase in lower-tropospheric water vapor due to warmer SSTs, a known consequence of anthropogenic greenhouse warming (e.g., Collins et al. 2013; Mizuta et al. 2014). In fact, the results in the present study indicate a close linkage between the intensification rate during the RI and the water vapor amount around the RMW (Fig. 11). Therefore, changes in an intense typhoon and the associated intensification process shown in the present study are most likely applicable to other intense TCs under warmer conditions.

6. Summary

To explore the impacts of future climate changes on the intensity and structures of an intense TC, we conducted numerical simulations of the most destructive historical TC to strike Japan, Typhoon Vera (1959), for the current climate and the future global warming climate with four 5-km-mesh nonhydrostatic models. Initial and boundary conditions for the control simulations of Typhoon Vera were provided by the JMA 55-year Reanalysis dataset. Future changes from the present-day period, 1979–2003, and the future period, 2075–99, were estimated by performing climate runs with a 20-km-mesh atmospheric general circulation model and then adding the results to the initial and boundary conditions of the control simulations.

The multimodel ensemble experiments produced robust signals showing that the maximum intensity of the typhoon increased in all warmer climate simulations (Table 2 and Fig. 3). The height and intensity of eyewall updrafts increased in all future simulations (Fig. 6). Similar changes have been suggested by idealized simulations (Shen et al. 2000; Hill and Lackmann 2011). However, our simulations were conducted by using the real synoptic environment of a historical intense TC, Typhoon Vera (1959). Furthermore, the results provided the additional information about structural changes that in a future TC the major changes appear within a radius of 100 km from the storm center (Fig. 5). These structural changes are accompanied by the continuous formation of intense eyewall updrafts inside the RMW (Fig. 9) and by contraction of the RMW during the rapid intensification phase. During that phase, a large

increase in the total solid water mixing ratio, which suggests latent heat release, occurs in the tall and intense eyewall updrafts, which formed continuously inside the RMW. The increase in near-surface inflow only around the eyewall region (Fig. 9d) suggests that enhancements of near-surface inflows and, hence, of the horizontal wind speed, are induced by strong diabatic heating in the vicinity of the eyewall.

There were, of course, some differences in the simulated intensities before the onset of rapid intensification. However, it is on the intensification process during the rapid intensification phase that future environment changes will have large impacts.

It should be noted that the PW approach cannot be used to project changes in the frequency or track of future TCs. Nonetheless, all four 5-km-mesh models projected that a future typhoon would intensify more rapidly as RMW contracted. Rapid contraction and the resultant smaller RMW imply rapid increases in the maximum wind speed in the vicinity of the RMW (Montgomery and Smith 2014). Thus, the present study results also show that people living in coastal regions in the future climate will need to take precautions against sudden increases in high winds and precipitation associated with the passage of intense TCs.

REFERENCES

Alvey, G. R., III, J. Zawislak, and E. Zipser, 2015: Precipitation properties observed during tropical cyclone intensity change. *Mon. Wea. Rev.*, **143**, 4476–4492, doi:10.1175/MWR-D-15-0065.1.

Bengtsson, L., K. I. Hodges, M. Esch, N. Keenlyside, L. Kornblueh, J.-J. Luo, and T. Yamagata, 2007: How may tropical cyclones change in a warmer climate? *Tellus*, **59A**, 539–561, doi:10.1111/j.1600-0870.2007.00251.x.

Cha, D. H., and Y. Q. Wang, 2013: A dynamical initialization scheme for real-time forecasts of tropical cyclones using the WRF Model. *Mon. Wea. Rev.*, **141**, 964–986, doi:10.1175/MWR-D-12-00077.1.

Charney, J. G., and A. Eliassen, 1964: On the growth of the hurricane depression. *J. Atmos. Sci.*, **21**, 68–75, doi:10.1175/1520-0469(1964)021<0068:OTGOTH>2.0.CO;2.

Christensen, J. H., and Coauthors, 2013: Climate phenomena and their relevance for future regional climate change. *Climate Change 2013: The Physical Science Basis*, T. F. Stocker et al., Eds., Cambridge University Press, 1217–1308.

Collins, M., and Coauthors, 2013: Long-term climate change: Projections, commitments and irreversibility. *Climate Change 2013: The Physical Science Basis*, T. F. Stocker et al., Eds., Cambridge University Press, 1029–1136.

Davis, C. A., 1992: Piecewise potential vorticity inversion. *J. Atmos. Sci.*, **49**, 1397–1411, doi:10.1175/1520-0469(1992)049<1397:PPVI>2.0.CO;2.

DeMaria, M., and J. Kaplan, 1994: Sea surface temperature and the maximum intensity of Atlantic tropical cyclones. *J. Climate*, **7**, 1324–1334, doi:10.1175/1520-0442(1994)007<1324:SSTATM>2.0.CO;2.

Dudhia, J., 1993: A nonhydrostatic version of the Penn State–NCAR Mesoscale Model: Validation tests and simulation of an Atlantic cyclone and cold front. *Mon. Wea. Rev.*, **121**, 1493–1513, doi:10.1175/1520-0493(1993)121<1493:ANVOTP>2.0.CO;2.

Emanuel, K. A., 1986: An air–sea interaction theory for tropical cyclones. Part I: Steady-state maintenance. *J. Atmos. Sci.*, **43**, 585–605, doi:10.1175/1520-0469(1986)043<0585:AASITF>2.0.CO;2.

——, 1988: The maximum intensity of hurricanes. *J. Atmos. Sci.*, **45**, 1143–1155, doi:10.1175/1520-0469(1988)045<1143:TMIOH>2.0.CO;2.

——, 2006: Subroutine to calculate the maximum wind speed and minimum central pressure achievable in tropical cyclone, given a sounding and a sea surface temperature. [Available online at ftp://texmex.mit.edu/pub/emanuel/TCMAX/pcmin_revised.f.]

Fierro, A. O., R. F. Rogers, F. D. Marks, and D. S. Nolan, 2009: The impact of horizontal grid spacing on the microphysical and kinematic structures of strong tropical cyclones simulated with the WRF-ARW Model. *Mon. Wea. Rev.*, **137**, 3717–3743, doi:10.1175/2009MWR2946.1.

Fudeyasu, H., and Y. Wang, 2011: Balanced contribution to the intensification of a tropical cyclone simulated in TCM4: Outer-core spinup process. *J. Atmos. Sci.*, **68**, 430–449, doi:10.1175/2010JAS3523.1.

Gentry, M. S., and G. M. Lackmann, 2010: Sensitivity of simulated tropical cyclone structure and intensity to horizontal resolution. *Mon. Wea. Rev.*, **138**, 688–704, doi:10.1175/2009MWR2976.1.

Gray, W. M., 1968: Global view of the origin of tropical disturbances and storms. *Mon. Wea. Rev.*, **96**, 669–700, doi:10.1175/1520-0493(1968)096<0669:GVOTOO>2.0.CO;2.

Grell, G. A., J. Dudhia, and D. Stauffer, 1994: A description of the fifth-generation Penn State/NCAR Mesoscale Model (MM5). NCAR Tech. Note NCAR/TN-398+STR, 128 pp., doi:10.5065/D60Z716B.

Hack, J. J., and W. H. Schubert, 1986: Nonlinear response of atmospheric vortices to heating by organized cumulus convection. *J. Atmos. Sci.*, **43**, 1559–1573, doi:10.1175/1520-0469(1986)043<1559:NROAVT>2.0.CO;2.

Hill, K. A., and G. M. Lackmann, 2011: The impact of future climate change on TC intensity and structure: A downscaling approach. *J. Climate*, **24**, 4644–4661, doi:10.1175/2011JCLI3761.1.

Holland, G. J., 1997: The maximum potential intensity of tropical cyclones. *J. Atmos. Sci.*, **54**, 2519–2541, doi:10.1175/1520-0469(1997)054<2519:TMPIOT>2.0.CO;2.

Holliday, C. R., and A. H. Thompson, 1979: Climatological characteristics of rapidly intensifying typhoons. *Mon. Wea. Rev.*, **107**, 1022–1034, doi:10.1175/1520-0493(1979)107<1022:CCORIT>2.0.CO;2.

Hong, S.-Y., Y. Noh, and J. Dudhia, 2006: A new vertical diffusion package with an explicit treatment of entrainment processes. *Mon. Wea. Rev.*, **134**, 2318–2341, doi:10.1175/MWR3199.1.

Hsiao, L. F., C. S. Liou, T. C. Yeh, Y. R. Guo, D. S. Chen, K. N. Huang, C. T. Terng, and J. H. Chen, 2010: A vortex relocation scheme for tropical cyclone initialization in Advanced Research WRF. *Mon. Wea. Rev.*, **138**, 3298–3315, doi:10.1175/2010MWR3275.1.

Ito, R., T. Takemi, and O. Arakawa, 2016: A possible reduction in the severity of typhoon wind in the northern part of Japan under global warming: A case study. *SOLA*, **12**, 100–105, doi:10.2151/sola.2016-023.

Janjić, Z. I., 1994: A step-mountain eta coordinate model: Further developments of the convection, viscous sublayer, and turbulence closure schemes. *Mon. Wea. Rev.*, **122**, 927–945, doi:10.1175/1520-0493(1994)122<0927:TSMECM>2.0.CO;2.

Kain, J., and J. Fritsch, 1993: Convective parameterization for mesoscale models: The Kain–Fritsch scheme. *The Representation of Cumulus Convection in Numerical Models*, *Meteor. Monogr.*, No. 24, Amer. Meteor. Soc., 165–170.

Kanada, S., and A. Wada, 2016: Sensitivity to horizontal resolution of the simulated intensifying rate and inner-core structure of typhoon Ida, an extremely intense typhoon. *J. Meteor. Soc. Japan*, **94A**, 181–190, doi:10.2151/jmsj.2015-037.

——, ——, and M. Sugi, 2013: Future changes in structures of extremely intense tropical cyclones using a 2-km mesh non-hydrostatic model. *J. Climate*, **26**, 9986–10 005, doi:10.1175/JCLI-D-12-00477.1.

Kaplan, J., and M. DeMaria, 2003: Large-scale characteristics of rapidly intensifying tropical cyclones in the North Atlantic basin. *Wea. Forecasting*, **18**, 1093–1108, doi:10.1175/1520-0434(2003)018<1093:LCORIT>2.0.CO;2.

Kawase, H., T. Yoshikane, M. Hara, F. Kimura, T. Yasunari, B. Ailikun, H. Ueda, and T. Inoue, 2009: Intermodel variability of future changes in the baiu rainband estimated by the pseudo global warming downscaling method. *J. Geophys. Res.*, **114**, D24110, doi:10.1029/2009JD011803.

Kieper, M., and H. Jiang, 2012: Predicting tropical cyclone rapid intensification using the 37 GHz ring pattern identified from passive microwave measurements. *Geophys. Res. Lett.*, **39**, L13804, doi:10.1029/2012GL052115.

Kimura, F., and A. Kitoh, 2007: Downscaling by pseudo global warning method. Research project on the impact of climate changes on agricultural production system in arid areas, Research Institute for Humanity and Nature Final Rep., 43–46.

Kitagawa, H., 2000: Radiation processes (in Japanese). JMA Numerical Prediction Division Tech. Rep. 46, 16–31.

Knabb, R. D., D. P. Brown, and J. R. Rhome, 2005: Tropical cyclone report: Hurricane Katrina, 23–30 August 2005. NOAA/NWS/NHC Rep., 43 pp. [Available online at http://www.nhc.noaa.gov/data/tcr/AL122005_Katrina.pdf.]

Knutson, T. R., and R. E. Tuleya, 1999: Increased hurricane intensities with CO_2-induced warming as simulated using the GFDL hurricane prediction system. *Climate Dyn.*, **15**, 503–519, doi:10.1007/s003820050296.

——, and ——, 2004: Impact of CO_2-induced warming on simulated hurricane intensity and precipitation: Sensitivity to the choice of climate model and convective parameterization. *J. Climate*, **17**, 3477–3495, doi:10.1175/1520-0442(2004)017<3477:IOCWOS>2.0.CO;2.

——, ——, W. Shen, and I. Ginis, 2001: Impact of CO_2-induced warming on hurricane intensities as simulated in a hurricane model with ocean coupling. *J. Climate*, **14**, 2458–2468, doi:10.1175/1520-0442(2001)014<2458:IOCIWO>2.0.CO;2.

——, and Coauthors, 2013: Dynamical downscaling projections of twenty-first-century Atlantic hurricane activity: CMIP3 and CMIP5 model-based scenario. *J. Climate*, **26**, 6591–6617, doi:10.1175/JCLI-D-12-00539.1.

——, and Coauthors, 2015: Global projections of intense tropical cyclone activity for the late twenty-first century from dynamical downscaling of CMIP5/RCP4.5 scenarios. *J. Climate*, **28**, 7203–7224, doi:10.1175/JCLI-D-15-0129.1.

Kobayashi, S., and Coauthors, 2015: The JRA-55 reanalysis: General specifications and basic characteristics. *J. Meteor. Soc. Japan*, **93**, 5–48, doi:10.2151/jmsj.2015-001.

Kondo, J., 1975: Air–sea bulk transfer coefficients in diabatic conditions. *Bound.-Layer Meteor.*, **9**, 91–112, doi:10.1007/BF00232256.

Lackmann, G. M., 2013: The south-central U.S. flood of May 2010: Present and future. *J. Climate*, **26**, 4688–4709, doi:10.1175/JCLI-D-12-00392.1.

——, 2015: Hurricane Sandy before 1900 and after 2100. *Bull. Amer. Meteor. Soc.*, **96**, 547–560, doi:10.1175/BAMS-D-14-00123.1.

Leslie, L. M., and G. J. Holland, 1995: On the bogussing of tropical cyclones in numerical models: A comparison of vortex profiles. *Meteor. Atmos. Phys.*, **56**, 101–110, doi:10.1007/BF01022523.

Lin, I.-I., and Coauthors, 2013: An ocean coupling potential intensity index for tropical cyclones. *Geophys. Res. Lett.*, **40**, 1878–1882, doi:10.1002/grl.50091.

Louis, J. F., M. Tiedtke, and J. F. Geleyn, 1982: A short history of the operational PBL parameterization at ECMWF. *Proc. Workshop on Planetary Boundary Layer Parameterization*, Reading, United Kingdom, ECMWF, 59–79.

Lynn, B. H., R. Healy, and L. M. Druyan, 2009: Investigation of Hurricane Katrina characteristics for future warmer climates. *Climate Res.*, **39**, 75–86, doi:10.3354/cr00801.

McFarquhar, G. M., B. F. Jewett, M. S. Gilmore, S. W. Nesbitt, and T.-L. Hsieh, 2012: Vertical velocity and microphysical distributions related to rapid intensification in a simulation of Hurricane Dennis (2005). *J. Atmos. Sci.*, **69**, 3515–3534, doi:10.1175/JAS-D-12-016.1.

Miyamoto, Y., and T. Takemi, 2013: A transition mechanism for the spontaneous axisymmetric intensification of tropical cyclones. *J. Atmos. Sci.*, **70**, 112–129, doi:10.1175/JAS-D-11-0285.1.

——, and ——, 2015: A triggering mechanism for rapid intensification of tropical cyclones. *J. Atmos. Sci.*, **72**, 2666–2681, doi:10.1175/JAS-D-14-0193.1.

Mizuta, R., and Coauthors, 2012: Climate simulations using MRI-AGCM with 20-km grid. *J. Meteor. Soc. Japan*, **90A**, 233–260, doi:10.2151/jmsj.2012-A12.

——, O. Arakawa, T. Ose, S. Kusunoki, H. Endo, and A. Kitoh, 2014: Classification of CMIP5 future climate responses by the tropical sea surface temperature changes. *SOLA*, **10**, 167–171, doi:10.2151/sola.2014-035.

Montgomery, M. T., and R. K. Smith, 2014: Paradigms for tropical cyclone intensification. *Aust. Meteor. Oceanogr. J.*, **64**, 37–66.

Mori, N., M. Kato, S. Kim, H. Mase, Y. Shibutani, T. Takemi, K. Tsuboki, and T. Yasuda, 2014: Local amplification of storm surge by Super Typhoon Haiyan in Leyte Gulf. *Geophys. Res. Lett.*, **41**, 5106–5113, doi:10.1002/2014GL060689.

Murakami, H., and M. Sugi, 2010: Effect of model resolution on tropical cyclone climate projections. *SOLA*, **6**, 73–76.

——, and Coauthors, 2012: Future changes in tropical cyclone activity projected by the new high-resolution MRI-AGCM. *J. Climate*, **25**, 3237–3260, doi:10.1175/JCLI-D-11-00415.1.

Nakamura, R., T. Shibayama, M. Esteban, and T. Iwamoto, 2016: Future typhoon and storm surges under different global warming scenarios: Case study of typhoon Haiyan (2013). *Nat. Hazards*, **82**, 1645–1681, doi:10.1007/s11069-016-2259-3.

Nakanishi, M., and H. Niino, 2004: An improved Mellor–Yamada level 3 model with condensation physics: Its design and verification. *Bound.-Layer Meteor.*, **112**, 1–31, doi:10.1023/B:BOUN.0000020164.04146.98.

Nakano, M., T. Kato, S. Hayashi, S. Kanada, Y. Yamada, and K. Kurihara, 2012: Development of a 5-km-mesh cloud-system-resolving regional climate model at the Meteorological Research Institute. *J. Meteor. Soc. Japan*, **90A**, 339–350, doi:10.2151/jmsj.2012-A19.

Needham, H. F., B. D. Keim, and D. Sathiaraj, 2015: A review of tropical cyclone–generated storm surges: Global data sources, observations, and impacts. *Rev. Geophys.*, **53**, 545–591, doi:10.1002/2014RG000477.

Nolan, D. S., 2007: What is the trigger for tropical cyclogenesis? *Aust. Meteor. Mag.*, **56**, 241–266.

Ooyama, K., 1969: Numerical simulation of the life cycle of tropical cyclones. *J. Atmos. Sci.*, **26**, 3–40, doi:10.1175/1520-0469(1969)026<0003:NSOTLC>2.0.CO;2.

Pendergrass, A. G., and H. E. Willoughby, 2009: Diabatically induced secondary flows in tropical cyclones. Part I: Quasi-steady forcing. *Mon. Wea. Rev.*, **137**, 805–821, doi:10.1175/2008MWR2657.1.

Rasmussen, R., and Coauthors, 2011: High-resolution coupled climate runoff simulations of seasonal snowfall over Colorado: A process study of current and warmer climate. *J. Climate*, **24**, 3015–3048, doi:10.1175/2010JCLI3985.1.

Reasor, P. D., R. Rogers, and S. Lorsolo, 2013: Environmental flow impacts on tropical cyclone structure diagnosed from airborne Doppler radar composites. *Mon. Wea. Rev.*, **141**, 2949–2969, doi:10.1175/MWR-D-12-00334.1.

Roberts, M. J., and Coauthors, 2015: Tropical cyclones in the UPSCALE ensemble of high-resolution global climate models. *J. Climate*, **28**, 574–596, doi:10.1175/JCLI-D-14-00131.1.

Rogers, R. F., P. Reasor, and S. Lorsolo, 2013: Airborne Doppler observations of the inner-core structural differences between intensifying and steady-state tropical cyclones. *Mon. Wea. Rev.*, **141**, 2970–2991, doi:10.1175/MWR-D-12-00357.1.

Rotunno, R., and K. A. Emanuel, 1987: An air–sea interaction theory for tropical cyclones. Part II: Evolutionary study using a non-hydrostatic axisymmetric numerical model. *J. Atmos. Sci.*, **44**, 542–561, doi:10.1175/1520-0469(1987)044<0542:AAITFT>2.0.CO;2.

——, and G. H. Bryan, 2012: Effects of parameterized diffusion on simulated hurricanes. *J. Atmos. Sci.*, **69**, 2284–2299, doi:10.1175/JAS-D-11-0204.1.

Saito, K., J. Ishida, K. Aranami, T. Hara, T. Segawa, M. Narita, and Y. Honda, 2007: Nonhydrostatic atmospheric models and operational development at JMA. *J. Meteor. Soc. Japan*, **85B**, 271–304, doi:10.2151/jmsj.85B.271.

Shen, W., R. E. Tuleya, and I. Ginis, 2000: A sensitivity study of the thermodynamic environment on GFDL model hurricane intensity: Implications for global warming. *J. Climate*, **13**, 109–121, doi:10.1175/1520-0442(2000)013<0109:ASSOTT>2.0.CO;2.

Skamarock, W. C., and Coauthors, 2008: A description of the Advanced Research WRF version 3. NCAR Tech. Note NCAR/TN-475+STR, 113 pp., doi:10.5065/D68S4MVH.

Stauffer, D. R., and N. L. Seaman, 1990: Use of four-dimensional data assimilation in a limited-area mesoscale model. Part I: Experiments with synoptic-scale data. *Mon. Wea. Rev.*, **118**, 1250–1277, doi:10.1175/1520-0493(1990)118<1250:UOFDDA>2.0.CO;2.

Stern, D. P., J. L. Vigh, D. S. Nolan, and F. Zhang, 2015: Revisiting the relationship between eyewall contraction and intensification. *J. Atmos. Sci.*, **72**, 1283–1306, doi:10.1175/JAS-D-14-0261.1.

Stowasser, M., Y. Wang, and K. Hamilton, 2007: Tropical cyclone changes in the western North Pacific in a global warming scenario. *J. Climate*, **20**, 2378–2396, doi:10.1175/JCLI4126.1.

Takayabu, I., K. Hibino, H. Sasaki, H. Shiogama, N. Mori, Y. Shibutani, and T. Takemi, 2015: Climate change effects on the worst-case storm surge: A case study of Typhoon Haiyan. *Environ. Res. Lett.*, **10**, 064011, doi:10.1088/1748-9326/10/6/064011.

Takemi, T., S. Nomura, Y. Oku, and H. Ishikawa, 2012: A regional-scale evaluation of changes in environmental stability for summertime afternoon precipitation under global warming from super-high-resolution GCM simulations: A study for the case in the Kanto Plain. *J. Meteor. Soc. Japan*, **90A**, 189–212, doi:10.2151/jmsj.2012-A10.

——, R. Ito, and O. Arakawa, 2016: Robustness and uncertainty of projected changes in the impacts of Typhoon Vera (1959) under global warming. *Hydrol. Res. Lett.*, **10**, 88–94, doi:10.3178/hrl.10.88.

Trapp, R. J., and K. Hoogewind, 2016: The realization of extreme tornadic storm events under future anthropogenic climate change. *J. Climate*, **29**, 5251–5265, doi:10.1175/JCLI-D-15-0623.1.

Tsuboki, K., and A. Sakakibara, 2002: Large-scale parallel computing of cloud resolving storm simulator. *High Performance Computing*, H. P. Zima et al., Eds., Springer, 243–259.

——, M. K. Yoshioka, T. Shinoda, M. Kato, S. Kanada, and A. Kitoh, 2015: Future increase of supertyphoon intensity associated with climate change. *Geophys. Res. Lett.*, **42**, 646–652, doi:10.1002/2014GL061793.

Ueno, M., 1989: Operational bogussing and numerical prediction of typhoon in JMA. JMA Numerical Prediction Division Tech. Rep. 28, 48 pp.

Vigh, J. L., and W. H. Schubert, 2009: Rapid development of the tropical cyclone warm core. *J. Atmos. Sci.*, **66**, 3335–3350, doi:10.1175/2009JAS3092.1.

Wang, W., and Coauthors, 2010: ARW version 3 modeling system user's guide. NCAR Mesoscale and Microscale Meteorology Division Rep., 312 pp.

Xu, J., and Y. Wang, 2010: Sensitivity of tropical cyclone inner-core size and intensity to the radial distribution of surface entropy flux. *J. Atmos. Sci.*, **67**, 1831–1852, doi:10.1175/2010JAS3387.1.

Yabu, S., S. Murai, and H. Kitagawa, 2005: Clear sky radiation scheme (in Japanese). JMA Numerical Prediction Division Rep. 51, 53–64.

Zhang, D.-L., and R. A. Anthes, 1982: A high-resolution model of the planetary boundary layer—Sensitivity tests and comparisons with SESAME-79 data. *J. Appl. Meteor.*, **21**, 1594–1609, doi:10.1175/1520-0450(1982)021<1594:AHRMOT>2.0.CO;2.

Zhu, P., and Coauthors, 2015: Impact of subgrid-scale processes on eyewall replacement cycle of tropical cyclones in HWRF system. *Geophys. Res. Lett.*, **42**, 10 027–10 036, doi:10.1002/2015GL066436.